Mathematical Biosciences and Engineering

MBE, 19(2): 2120–2146.
DOI: 10.3934/mbe.2022099
Received: 22 July 2021
Accepted: 27 October 2021
Published: 28 December 2021

http://www.aimspress.com/journal/MBE

Research article

Mechanical stress induces a scalable circularly polarized LEO satellite antenna with Quadrifilar spiral

Jie Shen[1,2,3,*,†], Han-min Liu[1,2,†] and Jing Wang[1,2]

[1] State Grid Jibei Zhangjiakou Wind and Solar Energy Storage and Transportation New Energy Co., Ltd, China
[2] Hebei Province Wind and Solar Energy Storage Combined Power Generation Technology Innovation Center, China
[3] Beijing University of Posts & Telecom, Beijing 100876, China

* **Correspondence:** Email: shenjie74@163.com; Tel: +08618901163698.

† These authors contributed equally to this work and should be considered co-first authors.

Abstract: This paper investigates a left-hand circularly polarized (LHCP) antenna and a right-hand circularly polarized (RHCP) antenna on LEO Satellite, which is based on the phase-tuning metasurface. We overcome its inherent limitations in size, weight and power, and designed a high-gain, ultra-lightweight, scalable antenna for small satellite communications. The antenna can generate continuous and large tunability of subwavelength, with low-Q resonators. The simulated and experimental results verify that different capacitance and inductance modes can be effectively generated by rotating the spiral arms of single-arm spiral antennas with corresponding degrees, which greatly simplify the feeding network. The maximum gain of the normal position within the angle of the uplink and downlink is 4~9 dBi higher than that of the ordinary polarized antenna. In addition, the design method proposed to this article is superior to the reference system in terms of impedance bandwidth, axial ratio bandwidth, and operation frequency. The performance achievements of this paper are implemented within the bandwidth of 3 MHz of uplink and downlink, such as impedance bandwidth is 3 MHz with impedance of 50, axial ratio bandwidth is 2.5 MHz, operation frequency of uplink is 240–243 MHz, downlink is 320 MHz and 401 MHz, and the voltage standing wave ratio (VSWR) is less than 2 dB which is so called S parameter, the above parameters can meet the performance index design requirements.

Keywords: circular polarization; spiral-type antenna; resonance; micro-electro-mechanical systems; tunable antenna; intermodal coupling; voltage standing wave ratio (VSWR)

1. Introduction

The Quadrifilar helical antenna has a heart-shaped circular polarization radiation pattern, maintains better circular polarization characteristics and high gain at a lower elevation angle, and has the advantages of simple and compact structure and independent of reference ground, has been widely used in satellite navigation and communication fields such as GPS and maritime communications [1,2]. The Quadrifilar helical antenna can obtain different shaped circularly polarized radiation patterns by adjusting its pitch radius ratio and the number of winding turns to meet different application requirements [3]. The Quadrifilar helical antenna can be realized by feeding two pairs of orthogonal double-arm spirals with equal amplitude 90° phase difference feeding, or in-phase feeding of the self-phase shift structure double-arm spiral; the Quadrifilar spiral antenna can be realized by metal wire [4]. It can also be rolled into a cylindrical or conical shape after printing on a flexible substrate [5].

In the engineering design of a wide-beam antenna, in addition to the realization of electrical performance indicators, it is also necessary to consider the space environment used and the level of processing and manufacturing technology [6]. Commonly used wide-beam antenna structures include microstrip patch antennas, choke horn antennas, Quadrifilar helical antennas and double-arm helical antennas, among which microstrip patch antennas have the advantages of low profile and lightweight [7]. However, the microstrip dielectric material cannot meet the anti-radiation characteristics of the space-time environment. The choke horn antenna is an all-metal structure that can achieve dual circular polarization, but it is too large to be used in the low band. The Quadrifilar helical antenna can achieve better electrical performance [8], but the feeding circuit is complicated, and a power divider circuit for sequential feeding needs to be specially designed. This increases the loss of the antenna and reduces the gain of the antenna. The dual-arm helical antenna has a simple structure, convenient power feeding, and small size, but its working bandwidth is relatively narrow [9]. It is usually necessary to install two antennas for receiving and transmitting to achieve the purpose of receiving and sending at the same time [10].

In this paper, coupled split-ring resonators (SRRs) are used to construct the electrically small antennas. The principal challenge for achieving reconfigurable optical antennas and metasurfaces is the need to generate continuous and large tunability of subwavelength, low-Q resonators [11]. We show that it is possible to exploit the modulated metasurface concept to control the unwanted coupling between antennas that are installed on the same satellite. A left-hand circularly polarized (LHCP) antenna and a right-hand circularly polarized (RHCP) antenna that are based on the phase-tuning metasurface are simulated and measured [12]. The radiation patterns of the proposed antenna illustrate the performance of left-handed circular polarization. The electromagnetic wave propagation of the antenna has conjugate symmetry, which shows equal and opposite phase distribution under left-handed circular polarization (LHCP) and right-handed circular polarization (RHCP) illumination [13]. Apply the propagation phase to decouple the conjugate response of the geometric phase and generate independent wavefronts in two cross-polarized output fields with LHCP and RHCP incident illumination [14]. The antennas used in practice (e.g., in geodetic sites) have lower cross-coupling at lower elevation angles, i.e., less attenuation on the LHCP signal for these elevations. Then the antenna design in this article adopts the LHCP method.

The simulated and experimental results verify that different capacitance and inductance modes can be effectively generated by rotating the spiral arms of single-arm spiral antennas with corresponding degrees, which greatly simplify the feeding network [15]. The test results demonstrated that this design could meet the requirements for attitude determination systems in low earth orbit satellites. Furthermore, an assembled antenna structure consisting of four-element geodesic antennas array is proposed for full 360° beam steering, which can operate in a broadband range from 0.8 GHz to 1.2 GHz. This structure imposes on them the electromagnetic character of a helical antenna [16].

2. Mathematics theory

2.1. Antenna design goals

The initial situation we assume involves a LEO platform and a user on-ground who demands to be informed about ship-related events in the shortest possible time [17]. Evaluating various use case scenarios, the following requirements were identified:

(1) Working frequency band: UHF;

(2) The working absolute bandwidth of the transceiver antenna: ± 10 MHz;

(3) The standing wave ratio of the transmitting and receiving antenna: VSWR ≤ 2;

(4) Transceiver antenna gain: Gain ≥ 2 dBic in the working frequency band, and the elevation angle is above 25° Gain ≥ −5 dBic;

(5) Polarization of transmitting and receiving antenna: right-hand circular polarization;

(6) Antenna size: diameter less than 160 mm, hollow 20 mm, height less than 320 mm.

2.2. Choice of antenna form

There are many types of common UHF satellite communication antennas, including planar microstrip antennas, crossed dipoles, and Quadrifilar helical antennas. These three types of antenna types have different characteristics and are suitable for different working environments and requirements [20]. When applied in a specific environment, the electrical performance of the antenna must meet the design requirements, and reasonable design of the antenna structure must be considered. For the wide-beam antenna required for this design [21], there is a height restriction when dual-frequency operation is ensured, and the size of the cross dipole is large and it is not a hollow structure, so it is not applicable. Although the microstrip antenna has a low profile, its radiation efficiency is low, and the gain decreases significantly beyond the elevation angle of ± 30°, which does not meet the required electrical performance requirements [20]. The helical antenna can be designed into a hollow structure, and has a wider beam, which is easy to work in combination. In summary, the helical antenna is the best choice. The following three types of dual-frequency helical antennas are designed, analyzed and compared, and a suitable antenna layout is selected [21].

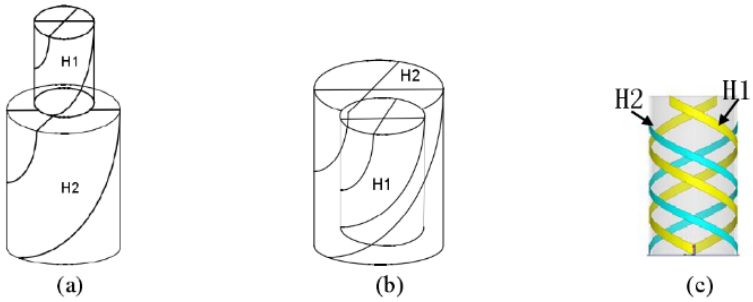

Figure 1. Three different dual-frequency helical antenna ideas.

As showed in Figure 1 above, three different implementation schemes for dual-frequency operation are drawn. The H1 part is an antenna working at high frequency, and the H2 part is an antenna working at low frequency [23]. Figure 1(a) Two Quadrifilar helical antennas stacked up and down. Due to the large size of the low-frequency antenna, in order to minimize the shielding of the antenna, the high-frequency antenna should be located on the upper layer, and the low-frequency antenna should be located on the lower layer; Figure 1(b) internal and external nesting type Quadrifilar helical antenna, the high-frequency antenna is small in size, it should be located in the inner circle, and the low-frequency is located in the outer circle; Figure 1(c) It is a co-cylinder compound double-arm helical antenna, the vibrator of the same frequency can be rotated 180° with one arm Coincident with the other arm [24].

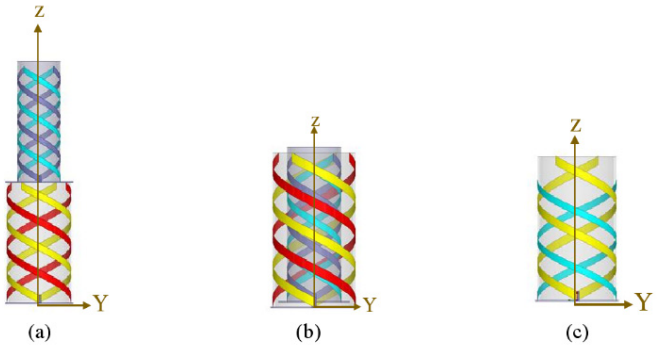

Figure 2. Three different dual-frequency helical antenna models.

Figure 2 shows the simulation models of three different dual-frequency helical antenna concepts. The height of the three antennas is 560 mm, 290 mm and 280 mm, respectively. Obviously, when the height of the model a is 0°, 45°, 90° and 135°, the gain difference of the pattern at an elevation angle of 25° is within ± 1 dB. The gain difference of the pattern c, while Phi = 0°, 45°, 90° and 135° at an elevation angle of 25° is greater than 4 dB, and the wide-angle gain at the angle without the feed arm is significantly smaller than other angles [25]. Therefore, this pattern of the model has poor symmetry.

2.3. Design principle of Quadrifilar helical antenna (QHA)

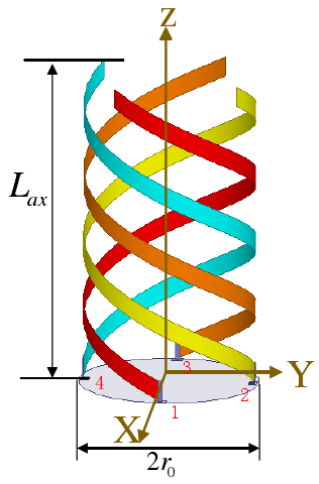

Figure 3. Schematic diagram of Quadrifilar helical antenna structure.

Figure 3 is a schematic diagram of the structure of a Quadrifilar helical antenna. The radiator of the antenna is composed of four spiral arms along the cylindrical surface opposite to the required circular polarization rotation of the antenna. The length of the spiral arm is $N/4$. When N is an odd number, the end of the spiral arm is open, and when N is an even number when the spiral arm ends are short-circuited [27]. The excitation of each arm of the vibrator is of equal amplitude and the phase difference is 90° in sequence.

The classic design equation of QHA is as follows:

$$L_{ax} = N\sqrt{\frac{L_{ele} - Ar_0}{N^2} - 4(\pi r_0)^2} \tag{1}$$

In Eq (1), L_{ele}: the length of the spiral arm, the length of the spiral arm is $\lambda/4$. When the odd number is multiple, A is 1, and when the even number is 2, L_{ax}: the height of the antenna, r_0: the radius of the antenna, N: the total antenna number of turns.

2.4. Polarized patch antenna array using metasurface

Furthermore, we propose the low radar cross section (RCS) circularly polarized patch antenna array operating at the downlink 400 MHz of the LEO satellite. Low RCS is achieved by replacing the conventional metallic ground with an artificial magnetic conductor (AMC)-based metasurface [27]. Two different AMC unit cells are designed having a phase difference within 180 ± 37° and combined in a chessboard-like configuration to realize the AMC-based metasurface. Moreover, the circular polarization (CP) performance is realized by embedding a circular slot on the patch radiator of the antenna element. The radiation characteristics of the antenna array are hardly impacted by the inclusion of the metasurface-based ground.

The reduction of RCS when plane waves are incident on metasurfaces of different AMCs can be approximated by the following equation, where θ_1, θ_2, B_1 and B_2 are the reflection sum coefficients

of. According to the equation, if the phase difference between unit cells is equal to 180, RCS reduction will be maximized.

$$\sigma(dBsm) = 10\lg\left[\left|\frac{B_1 e^{j\theta_1} + B_2 e^{j\theta_2}}{2}\right|^2\right]$$

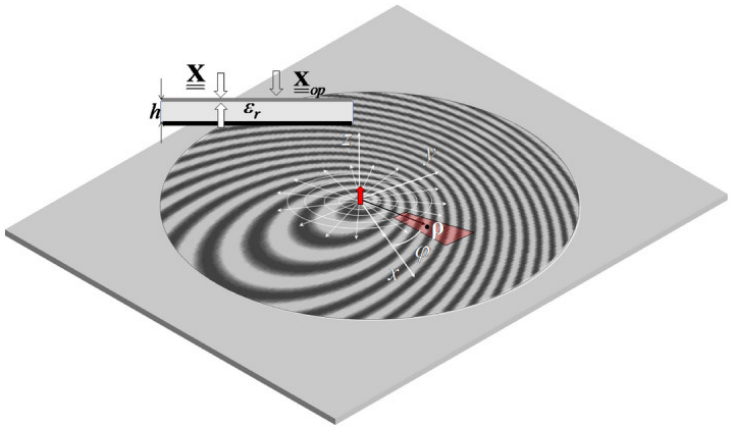

Figure 4. Geometry for the metasurface antenna.

From the optimal magnetic field position of the above equation, using the polar coordinated system(ρ,φ), the corresponding homogeneous reactance, the current flowing, and the coupling matrix of the array antenna can be calculated [28]. Figure 4 is a circular-domain meta-surface printed on a grounded dielectric slab. Where the $X(\rho)$ is the homogenized reactance and J is the electric current flowing, and ε_r is dielectric coefficient. The antenna is assumed be fed at its center ($\rho = 0$) with an elementary vertical dipole. Nevertheless, the methods adopted are also applicable for an arbitrary excitation, assuming the excitation fields are a priori known.

3. Antenna design and implementation

3.1. Design requirement

The upstream 240 MHz is located in the VHF frequency band, and the downstream 320 MHz and 400 MHz are located in the UHF frequency band. The uplink and downlink antennas are shared with transmission and reception, which requires an additional 28% of bandwidth, which makes it difficult to form a shaped beam. Therefore, the uplink and the downlink are designed to be separated from the transceiver to improve the isolation from the transceiver. In order to avoid the problems of beam reflection and occlusion, the antennas of the downlink UHF two frequency band are designed as an integrated receiver and transceiver.

(1) The terminal works in half-dual mode;

(2) Using circularly polarized antennas as the first choice. Linearly polarized antennas can also achieve equipment miniaturization.

The left circularly polarized antenna is adopted, and its parameters are as follows: Using left-hand circular polarization, standing wave ratio ≤ 2; characteristic impedance: 50 Ω; uses a

Quadrifilar spiral antenna.

The antenna floor is an antenna installation platform, and the coordinate zero point is located at the center of the platform. Forward direction is along the −Y axis direction, backward direction is along the +Y axis direction, left direction is along the +X axis direction, and the right direction is along the −X axis direction. The ground is parallel to the XOY plane, the +Z axis points to the zenith, the XOY plane is the H-plane of the antenna, and the YOZ plane is the E-plane of the antenna [28].

For convention: The H plane of the antenna is horizontal (XOY plane in Figure 4); The E plane of the antenna is vertical (YOZ plane in Figure 4).

3.2. Antenna structure

According to the requirements of technical indicators, within a given size range, the antenna has a high Q value, a narrow bandwidth, and the real part of the input impedance is generally small. Even if there are some resonance points, the imaginary part changes very sharply, so it is not easy to match.

Conventional microstrip antennas and arrays are not easy to achieve miniaturization. It is more difficult to form circular polarization, matching and polarization axis ratio is not good. Hence, the spiral structure is selected. The circular antenna height is tentatively set to 140 mm, and the vertical polarization antenna height is determined as 150 mm, adding distributed matching network to achieve working frequency resonance effect.

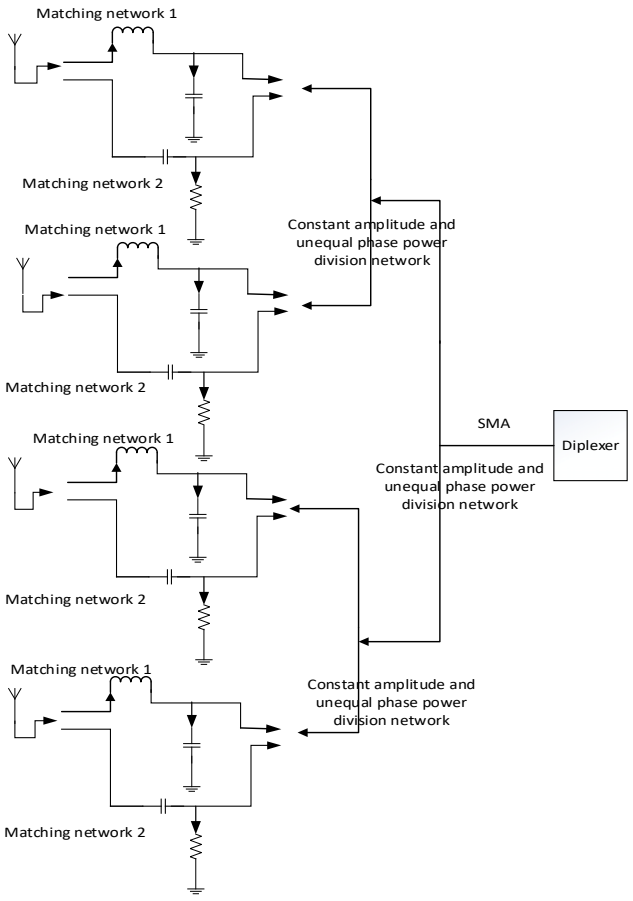

Figure 5. Quadrifilar spiral block diagram.

3.3. Analysis of feed form

The four arms of the circularly polarized antenna can realize 90-degree phase difference equal-amplitude output through three electric bridge, realize the circularly polarized resonance structure of the antenna, and optimize the matching circuit to improve radiation efficiency [29].

A single arm of a vertically polarized antenna is connected to a matching circuit on the back of the floor through a probe, and the radiation efficiency is improved by optimizing the matching circuit.

3.4. Antenna block diagram

When designing the antenna structure, the real part of the input impedance of the radiator is generally small, even at some resonance points, and the imaginary part changes very drastically, so it is not easy to match. And the radiation impedance is small at the weak resonance point (resulting in a small input impedance). Strong resonance point changes drastically, the bandwidth is very narrow, and the Q value is very high, causing the antenna to be non-resonant or low in efficiency [30]. This article guarantees the working frequency resonance when designing the antenna, and designs two matching networks corresponding to the two working frequencies. When circularly polarized antennas work, the four spiral arms are switched on and off to select two matching networks respectively, to achieve dual-frequency operation of the antenna within the size requirements.

Fesour antennas represent a spiral arm, which is directly connected to the gating switch. There are two matching networks behind the switch [31]. The two matching networks can respectively match the antenna to a working frequency, and achieve the effect of controlling the gating switch to select the working frequency. The feed network is followed by circular polarization of the antenna through a 90-degree bridge, which is finally connected to the transceiver through a SMA connector. Figure 4 is the Quadrifilar spiral block diagram.

4. Analysis of matching modes

The input impedance of a general antenna radiator is $Z = a + jb$, where a is the real part of the input impedance, which is generally small for small electrical antennas, and b is the imaginary part of the input impedance (positive number inductive, negative capacity). The characteristics of the small electric antenna are: the real part of the input impedance is generally small, even at some resonance points, it is relatively large, because the imaginary part changes very sharply, so it is not easy to match [32]. Hence, the characteristics of the small electric antenna are:

1) The radiation impedance is small at the weak resonance point (resulting in a small input impedance);

2) The distance of radiation impedance changes at a strong resonance point, and the bandwidth is very narrow;

3) The Q value is very high.

Among them, the weak resonance point means: as the frequency changes from low to high, the radiator port shows capacitive to inductive changes; the strong resonance point means: as the frequency changes from low to high, the radiator port shows inductive to capacitive changes [33]; The half-wave resonance point is generally a strong resonance point.

Antenna matching can be performed for strong resonance points or for weak resonance points [34]. The following three schemes are proposed for the two matching modes.

4.1. Series capacitor, parallel inductor mode

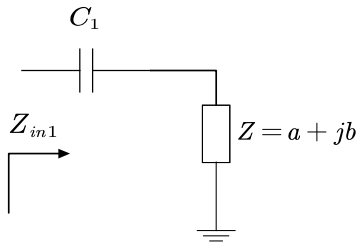

Figure 6. First level matches.

$$Z_{in1} = \frac{1}{j\omega C_1} + a + jb = a + j\left(b - \frac{1}{\omega C_1}\right) \tag{2}$$

The first-stage matching network being shown in Figures 6 and 7, is connected with a capacitor in series, so that the inductive part of the antenna radiator input impedance can be cancelled out, and the real part is unchanged [35]. For an antenna with a real input impedance close to 50 ohms, a capacitor can be connected in series at its input port. This can increase the resonance frequency.

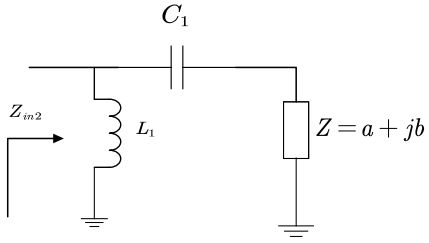

Figure 7. Second level match.

$$\begin{aligned} Z_{in2} &= \frac{1}{\frac{1}{j\omega L_1} + \frac{1}{Z_{in1}}} = \frac{j\omega L_1 \cdot Z_{in1}}{Z_{in1} + j\omega L_1} \\ &= \frac{(\omega L_1)^2 \cdot a}{a^2 + \left(b + \omega L_1 - \frac{1}{\omega C_1}\right)^2} + j\omega L_1 \cdot \frac{a^2 - \left(b + \omega L_1 - \frac{1}{\omega C_1}\right) \cdot \left(\frac{1}{\omega C_1} - b\right)}{a^2 + \left(b + \omega L_1 - \frac{1}{\omega C_1}\right)^2} \end{aligned} \tag{3}$$

To achieve matching, first the imaginary part must be zero and the real part must be 50 ohms:

$$\begin{cases} a^2 = \left(b + \omega L_1 - \frac{1}{\omega C_1}\right) \cdot \left(\frac{1}{\omega C_1} - b\right) \\ \frac{(\omega L_1)^2 \cdot a}{a^2 + \left(b + \omega L_1 - \frac{1}{\omega C_1}\right)^2} = 50 \end{cases} \tag{4}$$

Solve the equations in MATLAB to get the values of L_1 and C_1. And judge whether the solution is meaningful.

Assuming:

$$A(\omega) = \frac{(\omega L_1)^2 \cdot a}{a^2 + \left(b + \omega L_1 - \frac{1}{\omega C_1}\right)^2},$$
$$B(\omega) = \omega L_1 \cdot \frac{a^2 - \left(b + \omega L_1 - \frac{1}{\omega C_1}\right) \cdot \left(\frac{1}{\omega C_1} - b\right)}{a^2 + \left(b + \omega L_1 - \frac{1}{\omega C_1}\right)^2} \tag{5}$$

At this time, ω is a variable, and the others are constants. The values of L_1 and C_1 are substituted with solutions, and the bandwidth is determined according to the following equation:

$$P = \sqrt{\left(\frac{\partial(A(\omega))}{\partial\omega}\right)^2 + \left(\frac{\partial(B(\omega))}{\partial\omega}\right)^2}\Bigg|_{\omega=\omega_0} \tag{6}$$

where ω_0 is the current matches the angular frequency. The larger the value of P, the narrower the bandwidth.

4.2. Series inductor, parallel capacitor mode

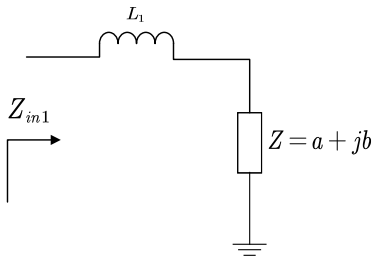

Figure 8. First level matches.

$$Z_{in1} = j\omega L_1 + a + jb = a + j(b + \omega L_1) \tag{6}$$

The first-stage matching network being shown in Figures 8 and 9, is connected in series with an inductor, so that the capacitive input impedance of the antenna radiator can be cancelled out, and the real part remains unchanged. For an antenna whose input impedance is close to 50 ohms, an inductor can be connected in series to its input port. This can reduce the resonance frequency.

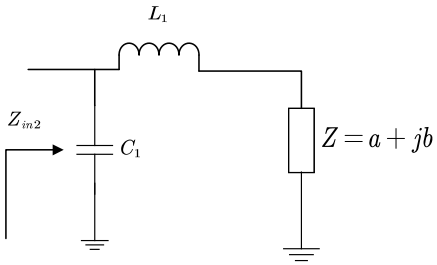

Figure 9. Second level matches.

$$Z_{in2}=\frac{1}{j\omega C_1+\frac{1}{Z_{in1}}}=\frac{Z_{in1}}{j\omega C_1\cdot Z_{in1}+1}=\frac{a}{(\omega aC_1)^2+[1-\omega C_1\cdot(b+\omega L_1)]^2}+j\frac{b+\omega L_1-\omega C_1\cdot(b+\omega L_1)^2-\omega a^2C_1}{(\omega aC_1)^2+[1-\omega C_1\cdot(b+\omega L_1)]^2}$$

To achieve matching, first the imaginary part must be zero, and the real part must be 50 ohms:

$$\begin{cases}(b+\omega L_1)\cdot(b+\omega L_1+\omega L_2)+a^2=0\\ \dfrac{a\omega^2L_2^2}{a^2+(b+\omega L_1+\omega L_2)^2}=50\end{cases}$$

Solve the equation in MATLAB to get the values of L_1 and C_1, and judge whether the solution is meaningful. Assume that:

$$A(\omega)=\frac{a}{(\omega aC_1)^2+(1-\omega C_1\cdot(b+\omega L_1))^2},$$
$$B(\omega)=\frac{b+\omega L_1-\omega C_1\cdot(b+\omega L_1)^2-\omega a^2C_1}{(\omega aC_1)^2+(1-\omega C_1\cdot(b+\omega L_1))^2}$$

At this time, ω is a variable, and the others are constants. The values of L_1 and C_1 are substituted with the solution, and the bandwidth is judged according to the following equation:

$$P=\sqrt{\left(\frac{\partial(A(\omega))}{\partial\omega}\right)^2+\left(\frac{\partial(B(\omega))}{\partial\omega}\right)^2}\Bigg|_{\omega=\omega_0}$$

Among them, ω_0 is the current matching angular frequency. The larger the value of P, the narrower the bandwidth.

4.3. Series inductance, parallel inductance mode

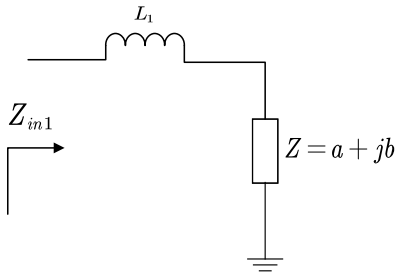

Figure 10. First level matches.

$$Z_{in1}=j\omega L_1+a+jb=a+j(b+\omega L_1)$$

The first-stage matching network being shown in Figures 10 and 11, is connected in series with an inductor, so that the capacitive input impedance of the antenna radiator can be cancelled out, and

the real part remains unchanged. For an antenna whose input impedance is close to 50 ohms, an inductor can be connected in series to its input port. This can reduce the resonance frequency.

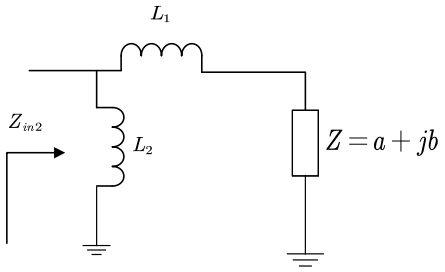

Figure 11. Second level matches.

$$Z_{in2} = \frac{1}{\frac{1}{j\omega L_2} + \frac{1}{Z_{in1}}} = \frac{j\omega L_2 \cdot Z_{in1}}{j\omega L_2 + Z_{in1}} = \frac{a\omega^2 L_2^2}{a^2 + (b + \omega L_1 + \omega L_2)^2} + j\frac{\omega L_2 \cdot (b + \omega L_1) \cdot (b + \omega L_1 + \omega L_2) + a^2 \omega L_2}{a^2 + (b + \omega L_1 + \omega L_2)^2}$$

This matching network is only suitable for matching capacitive networks, namely $b < 0$. To achieve matching, first the imaginary part must be zero, and the real part must be 50 ohms:

$$\begin{cases} (b + \omega L_1) \cdot (b + \omega L_1 + \omega L_2) + a^2 = 0 \\ \dfrac{a\omega^2 L_2^2}{a^2 + (b + \omega L_1 + \omega L_2)^2} = 50 \end{cases}$$

Solve the equation in MATLAB to get the values of L_1 and C_1, and judge whether the solution is meaningful. Assume that:

$$A(\omega) = \frac{a}{(\omega a C_1)^2 + (1 - \omega C_1 \cdot (b + \omega L_1))^2},$$
$$B(\omega) = \frac{b + \omega L_1 - \omega C_1 \cdot (b + \omega L_1)^2 - \omega a^2 C_1}{(\omega a C_1)^2 + (1 - \omega C_1 \cdot (b + \omega L_1))^2}$$

Here, ω is a variable, and the others are constants. The values of L_1 and C_1 are substituted with the solution, and the bandwidth is judged according to the following equation:

$$P = \sqrt{\left(\frac{\partial(A(\omega))}{\partial\omega}\right)^2 + \left(\frac{\partial(B(\omega))}{\partial\omega}\right)^2}\Bigg|_{\omega=\omega_0}$$

Among them, ω_0 is the current matching angular frequency. The larger the value of P, the narrower the bandwidth.

5. Simulation of Quadrifilar helical antenna radiator

The circularly polarized Quadrifilar helical antenna is realized within a reasonable size range, the working frequency band is good, the polarization method is left-hand circular polarization, the simulation axis ratio is low, the gain is greater than 0, and meets the technical index requirements; the vertical polarization single-arm helical antenna Within the specified size range, the standing wave of the working frequency band is good, the polarization mode is vertical linear polarization, the gain is greater than 0, and the technical index requirements are met.

5.1. Simulation model, environment and settings

5.1.1. Simulation model

The form of the circular polarization antenna is a Quadrifilar helical antenna. As showed in Figure 12, the antenna size is 140 mm × 140 mm × 140 mm, and the height does not exceed 0.12 wavelengths. It is an electrically small antenna. The four arms are of equal amplitude, and the phase difference is 90°. The reason for using a dielectric plate in the middle and using a four-wall spiral is to facilitate the formation of circular polarization, reduce the size of the antenna, and achieve the requirements for miniaturization of the antenna. Since the real part of the input impedance of a small antenna is generally small, and the imaginary part changes very sharply, it is not easy to match, and the uplink frequency band and the downlink frequency band are separated by a large distance. Therefore, a similar scheme shown in Figure 2 is required, and two matching networks are gated by switches. So that the antenna can achieve dual-frequency operation, and there is no upper limit for memory usage.

5.1.2. Standing wave ratio

Computer environment: (1) Processor: 8-core I7-7700K CPU, clocked at 4.20 GHz; (2) RAM 64 GHz; (3) 64-bit Windows 7 operating system. The model uses HFSS 15.0 software for simulation. In a single simulation, the software is set to 4 cores for simultaneous parallel calculation, and there is no upper limit for memory usage.

5.1.3. Parameter settings

(1) Convergence setting: The maximum number of model mesh updates is 20 times, and the convergence S error parameter is set to 2%;

(2) Boundary setting: set a square boundary setting at 350 mm from the outer boundary of the model, the main radiation direction is 350 mm from the top of the antenna, and the bottom boundary is

Table 1. Circular polarization antenna standing wave ratio simulation list.

Frequency band (MHz)	Technical index requirements	Simulation index	Meet the requirements
240	$\leqslant 2$	1.98	Y
243	$\leqslant 2$	1.88	Y
318	$\leqslant 2$	1.68	Y
320	$\leqslant 2$	1.32	Y

Three hundred and fifty mm from the antenna floor, the PML absorption layer is set outside the boundary, and the lowest frequency of the layer is set to 200 MHz;

(3) Feeding port setting: when calculating the four-wall helical antenna, one wave port is connected to the matching network to feed the radiator through a quarter-to-four equal amplitude 90-degree phase difference power divider, and the impedance is set to 50 ohms; Three-dimensional structure diagram of Quadrifilar helical antenna is shown on Figure 12. Four feedback interfaces are respectively located on the $\pm x, y$ axis, and the antenna has a stress induced spring along the z axis, which can be ejected and deployed in space.

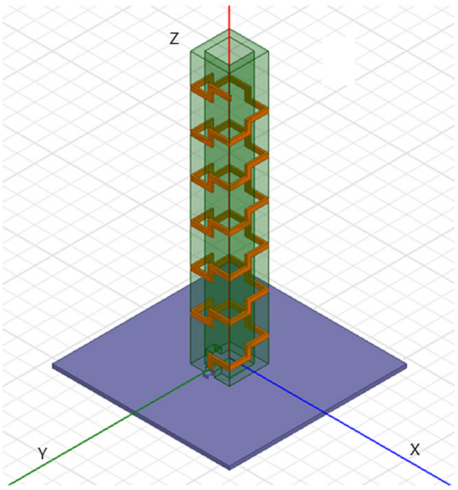

Figure 12. Quadrifilar helical antenna.

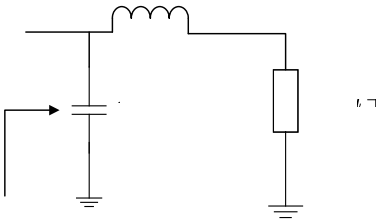

Figure 13. Matching network schematic simulation model.

(4) Material Setting: the helical antenna material is set to aluminum; the bottom antenna plate is set to aluminum, the dielectric board is the Rogers3010 board, and the environment material is air.

(5) Scan Setting: Set the frequency sweep range according to the frequency band requirements in the antenna's technical index requirements (Table 1).

5.2. Standing wave ratio

The standing wave ratios of the uplink frequency band and the downlink frequency band are shown in Figures 14 and 15. The standing wave ratio is less than 2 in 240 MHz~243 MHz and 318 MHz~320 MHz. VSWR is also a parameter that reflects the S_{11} parameter. They can easily calculate with each other.

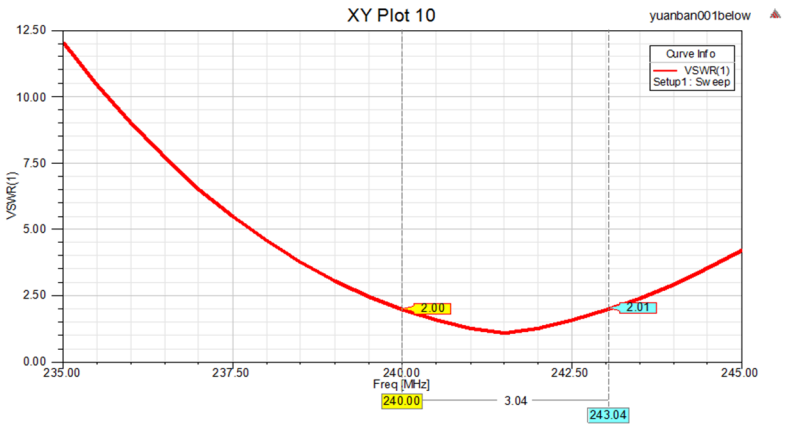

Figure 14. Transmission frequency standing wave ratio.

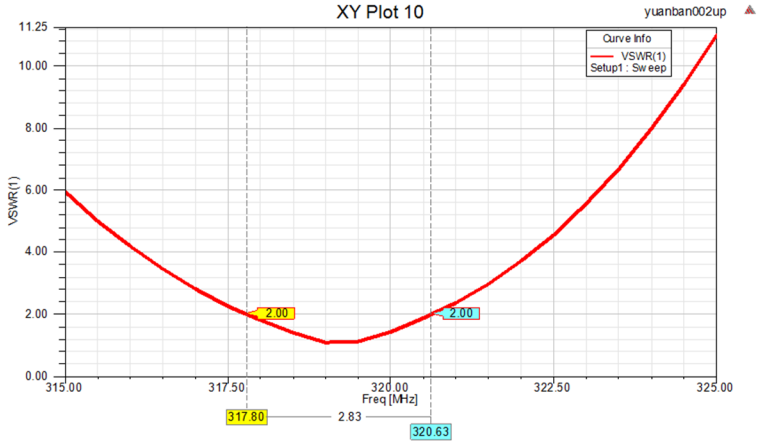

Figure 15. Receive frequency standing wave ratio.

The standing wave ratio data are sorted out as showing in Table 1. From the theoretical simulation, the standing wave ratio of the upper and lower frequency bands is close to 1, indicating that all the energy of the antenna is transmitted.

5.3. Gain and pattern, axis ratio

Figure 5 shows the simulation model diagram of the circularly polarized antenna, and Figures 6–10 are the 2D pattern of the H and E planes in the uplink frequency band and the downlink frequency band, and 3D type polarization gain diagrams. Figures 12 and 13 are the axial ratio patterns of the uplink frequency band and the lower frequency band, respectively. Each gain is the gain value after considering the dielectric loss of the model and the standing wave loss. However, due to the limitations of the simulation model, the insertion loss caused by factors such as cables, shunts, connectors, and randoms is not considered, and an overall study is needed. Figures 16–23 shows the simulation results.

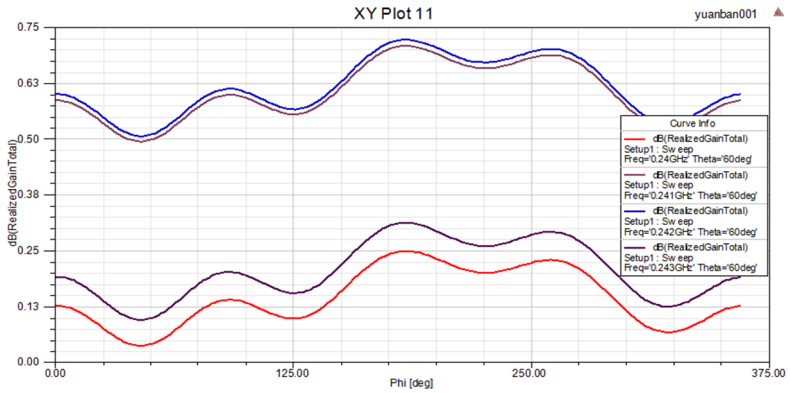

Figure 16. The H-plane main polarization pattern of the uplink frequency band.

Figure 16 shows the polarization performance of the magnetic field that is H-plane at 240 MHz uplink. This figure is a simulated circularly polarized antenna, using a spherical polar coordinate system, and θ=60° is the angle between the line segment and the positive direction of the z-axis. It can be seen that the magnetic field intensity on different frequencies is the largest near the XOZ planed tripod φ=180°,270°.

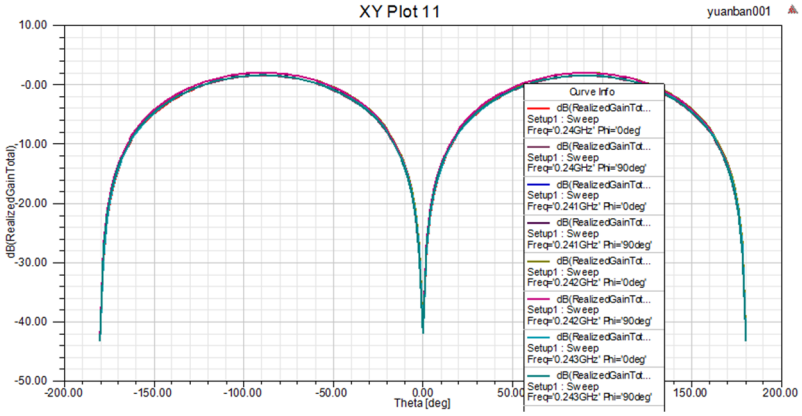

Figure 17. The E-plane main polarization pattern of the uplink frequency band.

Figure 17 shows the polarization performance of the electric field that is E-plane at 240 MHz uplink. This figure is also simulated in spherical coordinating, and the result shows that the electric field intensity, which is the largest at $\theta=\pm 90°$.

Figure 18 shows the polarization performance of the magnetic field that is H-plane at 320 MHz uplink. The maximum value of the intensity of the magnetic field polarization mode is 175°, and the minimum value is near 315°.

Figure 19 shows the polarization performance of the electric field that is E-plane at 240 MHz uplink. The polarization intensity of the electric field in the downward direction has the maximum value of ±90°, which is the same as that in the upward direction.

Figure 20 shows the main 3D polarization pattern of uplink and downlink at 240 MHz and 320 MHz respectively. The maximum gain of the circularly polarized antenna are in the XOY plane.

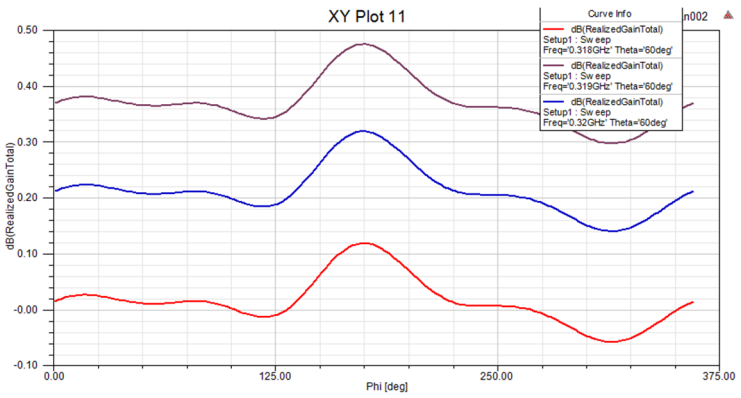

Figure 18. H-plane main polarization pattern in the downlink frequency band.

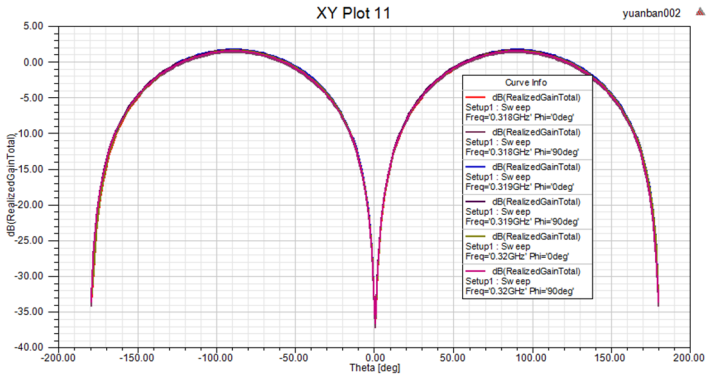

Figure 19. Main polarization pattern of E-plane in the downlink frequency band.

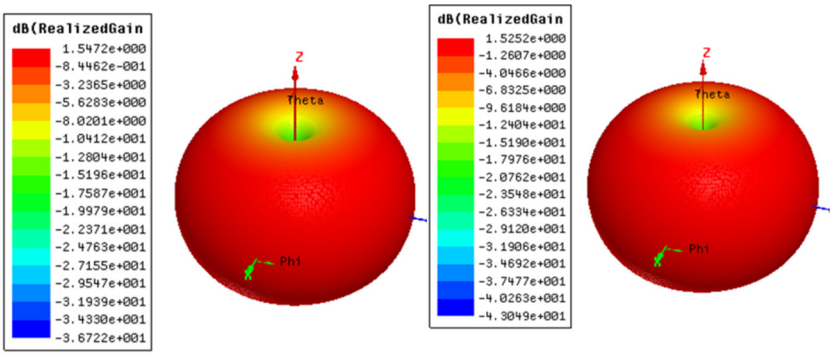

Figure 20. 3D main polarization pattern of uplink and downlink frequency bands.

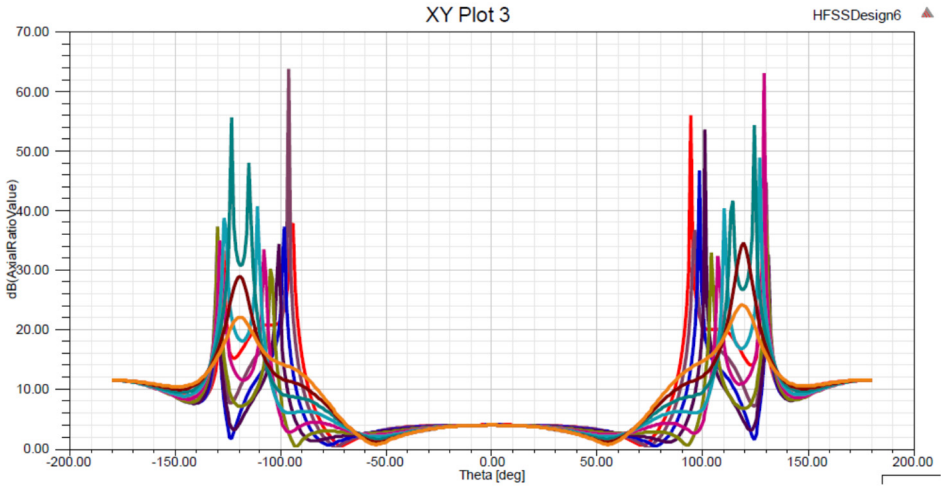

Figure 21. Axial ratio pattern of main polarization gain in uplink frequency band (240 MHz).

Figure 21 is the axial ratio pattern of main polarization gain in uplink at 240 MHz frequency band.

The definition of the axial ratio of the antenna: the trajectory of the endpoint of the instantaneous electric field vector of any polarized wave is an ellipse, and the ratio of the long axis to the short axis of the ellipse is called the axial ratio AR (axial ratio). The axial ratio is an important performance index of a circular polarization antenna. It represents the purity of the circular polarization. The bandwidth of the axial ratio not greater than 3 dB is defined as the circular polarization bandwidth of the antenna. It is an important indicator to measure the difference between the signal gain of the whole machine in different directions. The axial ratio is the ratio of the long axis to the short axis of the polarization ellipse. Obvious peaks appear near $\theta = 120$, indicating that these directions have changed from circular polarization to linear polarization.

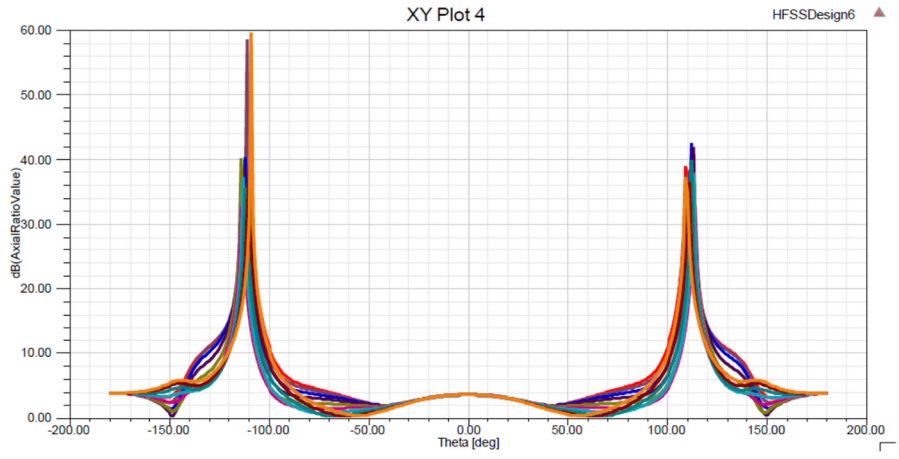

Figure 22. Axial ratio pattern of main polarization gain in downlink frequency band (320MHz).

Figure 22 is the axial ratio pattern of main polarization gain in downlink at 320 MHz frequency band. Obvious peaks appear near $\theta = \pm 110^{\circ}$, indicating that these directions have changed from

circular polarization to linear polarization.

5.4. Antenna test conclusion

The Quadrifilar helical antenna is in the working frequency band, the port standing wave is less than 2, the gain is ≥ 2.5 dBi, the beam width with an axial ratio of less than 3 dB is about –70°~70°, and the size is 140 mm × 140 mm × 140 mm, all indicators meet the design requirements.

The antenna standing wave ratio test uses a network vector analyzer. The antenna radiation characteristic test is carried out in a microwave anechoic chamber, equipped with a far-field test system consisting of a signal source, a signal receiver, a rotating platform, and analysis software.

Follow figures are test equipment used for the standing wave ratio test (a) and antenna radiation characteristic test (b) respectively. Figures 25–28 shows the test results.

Figure 23 is the photo of the actual antenna prototype, and Figure 24 is measurement facilities for the far field. The polarization mode, gain, and beam width of the helical antenna belongs to the radiation characteristic, all can be tested for the far-field test system (b), measurement facilities for the far field test are showed in (c).

(1) The voltage standing wave ratio (VSWR) tests procedure is as following:

a) Set the network analyzer to test the working frequency and signal powered level, the signal power level is –15 dBm;

b) Perform single-port calibration on Port1 of the network analyzer in the frequency range of 200 MHz~600 MHz;

c) Connect the receiving antenna unit input interface to the calibrated network analyzer port, as shown in Figure 24(a);

d) Set the measurement item to S_{11} (the S parameter), the output formats of VSWR, and record the standing wave ratio of the antenna at each frequency.

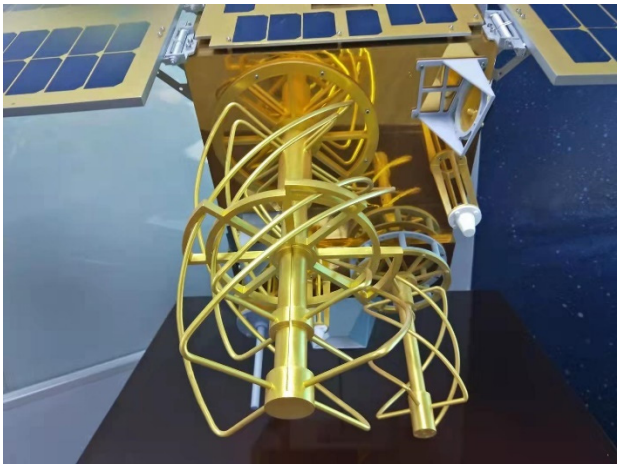

Figure 23. The photo of the actual antenna prototype.

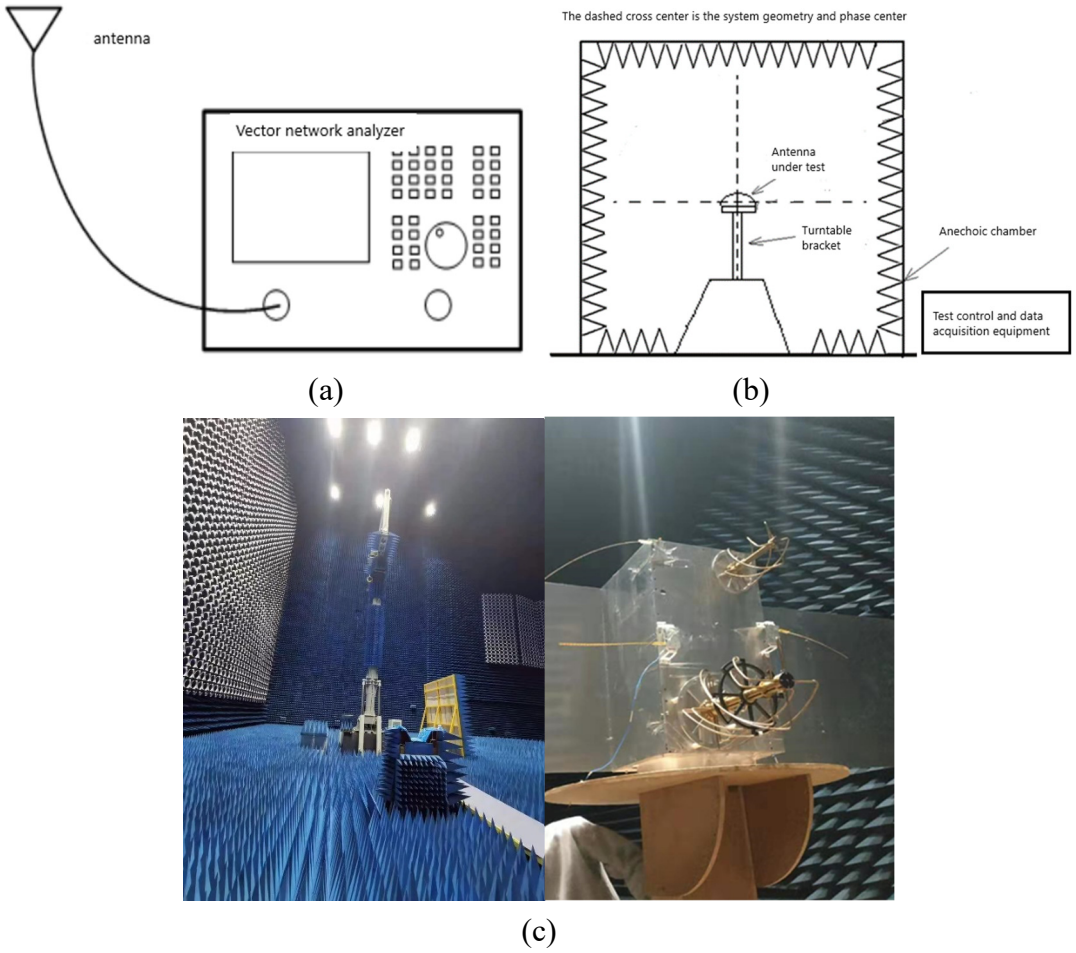

Figure 24. Measurement facilities for the far field.

(2) The Antenna radiation characteristic test and its operation steps are as following:

The polarization mode, axial ratio, gain, and beam width of the four-arm helical antenna belongs to the radiation characteristic test of the antenna, and can be tested in the far-field test system. The vertical polarization antenna index tested realization parameters are listed on Table 2. The test diagram is shown in Figure 24(b).

a) Install the standard gain horn antenna of the corresponding frequency of the test turntable, and adjust the horn mouth surface to a horizontal state with a level meter;

b) Measuring standard gains horn antenna: Rotate the measurement turntable, and the data acquisition system will automatically collect measurement data (Theta: –180~+180°, phi: 0, 90°, every 0.5°), save the measurement data and form a file, For post-processing use;

c) Remove the measured standard gains horn, install the antenna to be tested for the measurement turntable, and level the antenna surface; rotate the measurement turntable, and the measurement data will be automatically collected by the data acquisition system (Theta: –180~+180°, phi: 0, 90°, every 0.5°), save the measurement data and form a file for post-processing;

d) After the measurement is completed, remove the antenna, perform data processing, import the test data onto the standard horn and the test data onto the antenna to be tested for the test software, and export the far-field test data onto the entire beam of the antenna to be tested;

5) Perform data processing on the far-field test data to obtain the required data and draw it into a graph.

Table 2. Vertical polarization antenna index realization list.

No.	Performance	Requirement index	Design index
1	Frequency band	318 MHz~320 MHz; 240 MHz~243 MHz	318 MHz~320 MHz; 240 MHz~243 MHz
2	Voltage standing wave ratio	< 2	2
3	Impedance	50 Ω	50 Ω
4	Size	≤ 30 mm × 30 mm × 150 mm	≤ 30 mm × 30 mm × 150 mm
5	Polarization gain	≥ 0 dBi	≥ 0 dBi

Figure 23 is the test result of the antenna gain pattern of the uplink at 241 MHz. As can be seen from the above figure, the antenna gain has the maximum value in the range of $0°$ and $90°$. These results agreed well with the simulation results of Figures 16 and 17, that the maximum values are obtained at $\pm 90°$, $180°$ and $270°$ respectively.

Figure 24 is the test result of the antenna gain pattern of the downlink at 320 MHz. As can be seen from the above figure, the antenna gain has the maximum value in the range of $\varphi = 0°$ and $90°$. These results agreed well with the simulation results of Figures 18 and 19, that the maximum values is obtained at $\pm 90°$ respectively.

Figure 25 is the test result of the antenna gain pattern of the downlink at 401.5 MHz. As showed in the figure above, the antenna gain of 401.5 MHz in the downlink direction is also at $\varphi = 0°$ and $90°$, and the maximum value is obtained.

Figure 26 is the antenna standing wave ratio of uplink at 240 MHz, and in the downlink at 320 MHz respectively. This figure shows the VSWR, and it is present the S parameter. As can be seen from the figure, at 320 MHz it basically shows that the energy is completely emitted, but at near 240 MHz, the standing wave ratio is 1.8, and it is still relatively large.

Through simulation and testing, the following conclusions are reached:

Since the height of the 240 Mhz deployed antenna is relatively high, stars and other antennas have no effect on its performance. The antenna forms a good earth-shaped beam with a gain of more than 3.95 dBi at an angle of ± 60°. The gain in the 0° direction (to the center of the earth) is better than 1dBi. The standing wave is better than 1.2, and the axial ratio is better than 5dB within ± 60°.

The performance simulation results of the antenna in the 320MHz frequency band: the standing wave is better than 2, the axial ratio is less than 5.2 dB in the range of ± 60°, and the antenna gain is better than −0.32 dBi in the range of ± 60°. Considering engineering realization, it is better than −1dBi; the antenna gain reaches 4 dBi at the normal position of 0°.

According to the on-orbit empirical test, the downlink margin of the 320 MHz frequency band is relatively large, and the margin is greater than 9 dBi. The antenna index fully meets the link requirements.

The performance simulation results of the antenna in the 401 MHz frequency band: the standing wave is better than 1.8, the axial ratio is less than 6.9dB in the range of ± 60°, and the antenna gain is better than −0.2 dBi in the range of ± 60°. Considering engineering realization, it is better than −1dBi; The antenna gain reaches 4.5 dBi at the normal position of 0°.

We list the comparison of the performances of the LHCP with other published works. The antenna size of this design is x 0.1 m, y 0.1 m and z 0.5 m in 3 dimensions respectively. The lower and higher

frequency bands for both impedance bandwidth and axial ratio bandwidth are 240 MHz and 243 MHz.

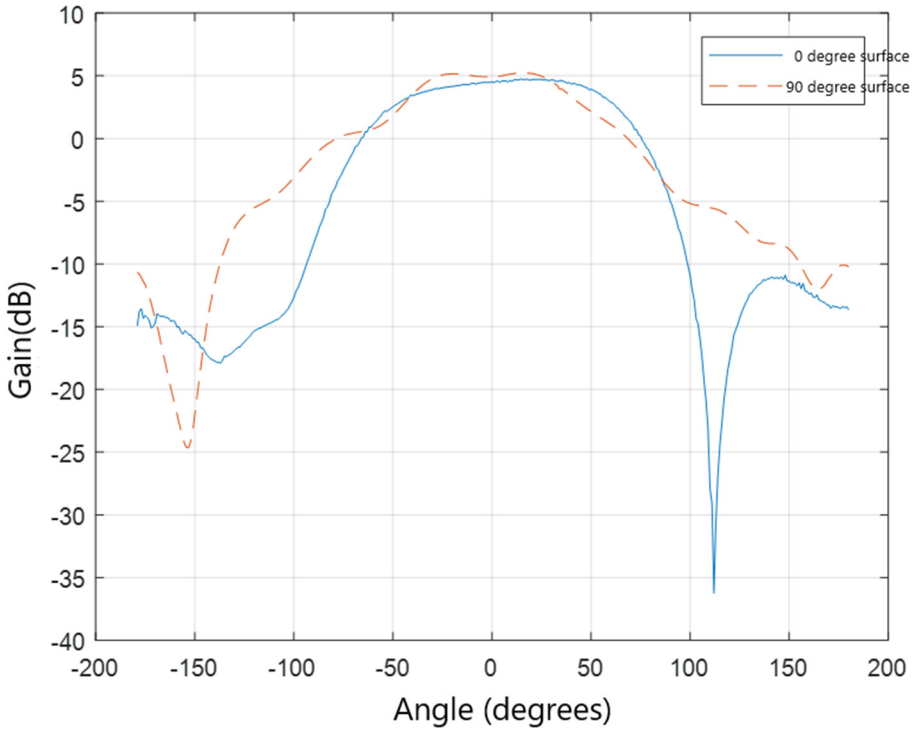

Figure 25. 241 MHz antenna pattern.

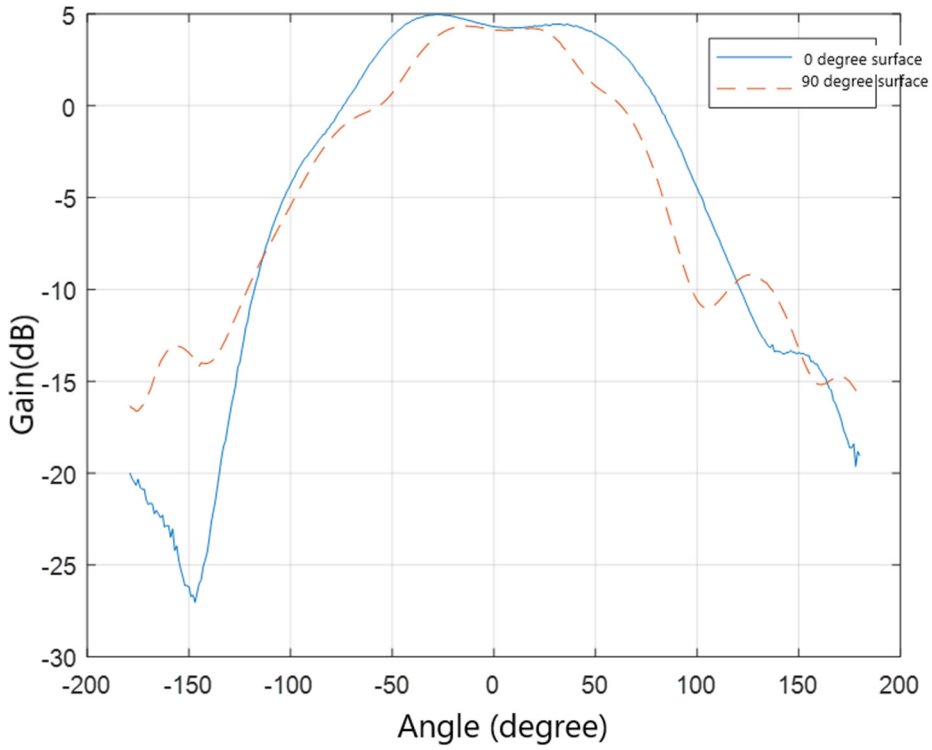

Figure 26. 320 MHz antenna gain pattern.

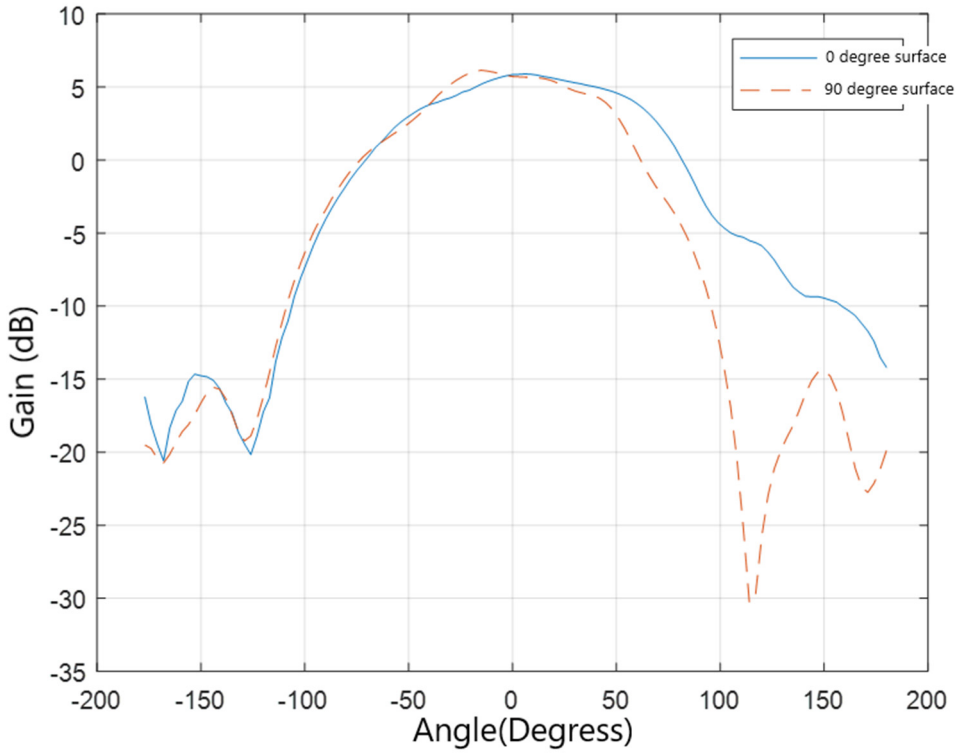

Figure 27. 401.5 MHz antenna gain's patterns.

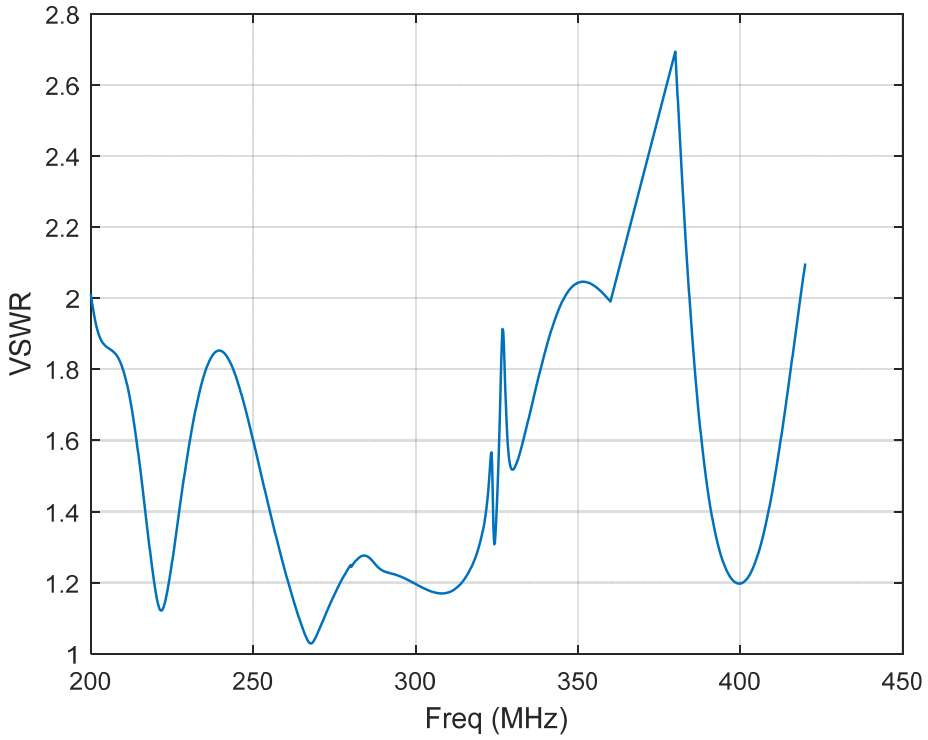

Figure 28. 240 MHz, 320 MHz antenna standing wave ratio.

Table 3. The comparison of LHCP with other works.

The reference	Antenna size	Impedance bandwidth	Axial ratio bandwidth	Gains	Radiation patterns
[13]	1 m	5 MHz	3 MHz	10.6 dBi	± 65°
[14]	0.75 m	5 MHz	2.8 MHz	13.5 dBi	± 65°
[15]	0.5 m	5 MHz	2.8 MHz	12.6 dBi	± 60°
[16]	0.5 m	3 MHz	2 MHz	13.5 dBi	± 50°
[17]	0.5 m	3 MHz	2 MHz	14 dBi	± 50°
This design	0.5 m	3 MHz	2.5 MHz	5 dBi	± 60°

6. Conclusions

The multi-frequency composite antenna proposed in this paper adopts multiple structural combinations of coplanar nesting, inner and outer nesting, and upper and lower combination, and combines the miniaturization of the antenna and the broadening beam technology to realize the multi-band composite work of UHF satellites. This nested composite antenna solution greatly reduces the overall physical height of the antenna while maintaining good antenna performance. In this paper, a total of three sets of wide-beam circularly polarized antennas covering six frequency bands are designed. First, the dual-frequency composite antenna of the UHF frequency band adopts the form of a nested four-arm antenna inside and outside, which ensures the wide beam characteristics of the antenna in the required frequency band. Another difficulty of this combination antenna is to design the feeder in a very narrow space. The electric network adopts a sub-type electric bridge, and adopts a double-layer cascaded feeder network, which realizes the miniaturization of the feeder network.

Table 4. Results of the proposed technique to be compared with reporting structures.

Structure	Wave ratio	Maximum gain (dBic)	Elevation angle
Prototype	< 1.5	> −2.6	25°
Composite antennas	< 1.5	> −3.3	25°
Metasurface Spiral type	< 1.5	> −2.7	25°

Table 4 presents comparing results of proposed spiral type technique with the reported prototype add composite antenna. It shows that under the same condition, the circularly polarized has optimal maximum gain. The test results of the antenna prototype show that the UHF antenna is in the required frequency band, the standing wave ratio is less than 1.5, and the gain is greater than −2.6 dBic at an elevation angle of 25°. Second, this paper designs composite antennas in the S and L frequency bands, and proposes a four-fed distributed antenna. The two frequency bands use the same flat antenna form, which reduces the profile antenna height. The test results of the antenna prototype show that the standing wave ratio of the antenna is less than 1.5 in the working frequency band, and the gain is greater than −3.3 dBic above the elevation angle of 25°. Third, for the antenna of Maritime Satellite Communication, the combined antenna of Archimedes spiral and equiangular spiral is used as the radiator, and the exponential gradient line balun is used as the feed structure. The test results of the antenna prototype show that the standing wave ratio of the antenna is less than 1.5 in the working frequency band, and the gain is greater than −2.7 dBic at an elevation angle of 25°. Since this design

has adopted mechanical stress induces a scalable, which can be deployed after the satellite enters the orbit, and its expansion and quality factor Q are adjustable. With this design, the antenna has a larger gain compared the result of article [36].

Acknowledgments

This project is funded by the State Grid Key Project "key technology of scale engineering application of power battery for echelon utilization", the project number is: 52010119002F.

Author contributions

These authors Jie Shen, Wenqi Dong and Jing Wang， contributed to the work equally and should be regarded as co-first authors.

Conflict of interest

We declare that we have no financial and personal relationships with other people or organizations that can inappropriately influence our work, there is no professional or other personal interest of any nature or kind in any product, service and/or company that could be construed as influencing the position presented in, or the review of, the manuscript entitled.

References

1. J. Gou, T. Zhang, J. Wang, Y. Jiang, Spiral antenna-coupled microbridge structures for THz application, *Nanoscale Res. Lett.*, **12** (2017), 91. doi: 10.1186/s11671-017-1857-7.
2. G. Rui, D. C. Abeysinghe, R. L. Nelson, Q. Zhan, Demonstration of beam steering via dipole-coupled plasmonic spiral antenna, *Sci. Rep*., **3** (2013), 1–7. doi: 10.1038/srep02237.
3. T. Alam, A. F. Almutairi, M. Samsuzzaman, M. Cho, M. T. Islam, Metamaterial array based meander line planar antenna for cube satellite communication, *Sci. Rep.*, **11** (2021), 1–12. doi: 10.1038/s41598-021-93537-6.
4. Y. Zhu, W. Dang, X. Liu, Y. Chen, X. Zhou, H. Lu, Generation of plane spiral orbital angular momentum using circular double-slot Vivaldi antenna arra, *Sci. Rep.*, **10** (2020), 1–9. doi:10.1038/s41598-020-75202-6.
5. H. Dai, W. Tao, J. Zhang, Design of compact circular polarization Quadrifilar spiral antenna for RFID, *Electron. Meas. Technol.*, **2017** (2017).
6. B. Ma, F. Lu, G. Zhi, X. Xue, X. Zhao, C. Ma, et al., Development of an X-band reflectarray antenna for satellite communications, *Sci. Rep.*, **11** (2021), 1–9. doi: 10.1038/s41598-021-85132-6.
7. A. Altaf, J. W. Jung, Y. Yang, K. Y. Lee, K. C. Hwang, Vertical-strip-fed broadband circularly polarized dielectric resonator antenna, *Sensors*, **17** (2017), 1911. doi:10.3390/s17081911.
8. T. T. Le, H. Y. Park, T. Y. Yun, Simple reconfigurable circularly polarized antenna at three bands, *Sensors*, **9** (2019), 2316. doi:10.3390/s19102316.

9. E. Arnaud, L. Huitema, R. Chantalat, A. Bellion, T. Monediere, Circularly polarized ferrite patch antenna for LEO satellite applications, *Int. J. Microwave Wireless Technol.*, **12** (2020), 332–338. doi: 10.1017/S1759078719001429.
10. M. Matsunaga, A linearly and circularly polarized double-band cross spiral antenna, *IEICE Trans. Commun.*, **99** (2016), 430–438. doi: 10.1587/transcom.2015EBP3222.
11. D. Rice, *A Circularly Polarized Tapered Spiral Cross-Slot Antenna*, 2017. Available from: https://digitalcommons.georgiasouthern.edu/research_symposium/2017/2017/89.
12. S. Wu, Y. Liu, G. Radice, S. Tan, Autonomous pointing control of a large satellite antenna subject to parametric uncertainty, *Sensors*, **17** (2017), 560. doi:10.3390/s17030560.
13. Y. Letestu, A. Sharaiha, Broadband folded printed Quadrifilar helical antenna, *IEEE Trans. Antennas Propag.*, **54** (2006), 1600–1604. doi: 10.1109/TAP.2006.874365.
14. K. S. Rao, D. R. Jahagirdar, Quadrifilar helical antenna with integrated compact feed for TTC application in LEO satellite, in *2018 IEEE Indian Conference on Antennas and Propogation (InCAP)*, (2018), 1–4.
15. C. Mengmeng, H. Weina, A printed Quadrifilar-helical antenna for Ku-band mobile satellite communication terminal, in *2017 IEEE 17th International Conference on Communication Technology (ICCT)*, (2017), 755–759.
16. P. Rezaei, Design of Quadrifilar helical antenna for use on small satellites, in *IEEE Antennas and Propagation Society Symposium*, (2004), 2895–2898.
17. N. Bhuma, C. Himabindh, Right hand circular polarization of a Quadrifilar helical antenna for satellite and mobile communication systems, in *Recent Advances in Space Technology Services and Climate Change 2010 (RSTS & CC-2010)*, (2010), 307–310.
18. H. Nakano, T. Shimizu, H. Kataoka, J. Yamauchi, Circularly and linearly polarized waves from a metamaterial spiral antenna, in *2014 IEEE Antennas and Propagation Society International Symposium (APSURSI)*, (2014), 535–536.
19. M. Liu, Y. Yuan, J. Ou, Y. Chai, Research on attitude models and antenna phase center correction for Jason-3 satellite orbit determination, *Sensors*, **19** (2019), 2408. doi:10.3390/s19102408.
20. L. Li, X. Zhou, Mechanically reconfigurable single-arm spiral antenna array for generation of broadband circularly polarized orbital angular momentum vortex waves, *Sci. Rep*., **8** (2018), 1–9. doi: 10.1038/s41598-018-23415-1.
21. J. Hong, R. Tu, R. Zhang, L. Fan, P. Zhang, J. Han, et al., Analyzing the satellite-induced code bias variation characteristics for the BDS-3 Via a 40 m dish antenna, *Sensors*, **20** (2020), 1339. doi:10.3390/s20051339.
22. Y. I. Abdulkarim, L. Deng, H. N. Awl, F. F. Muhammadsharif, O. Altintas, M. Karaaslan, et al., Design of a broadband coplanar waveguide-fed antenna incorporating organic solar cells with 100% insolation for Ku band satellite communication, *Materials*, **13** (2020), 142. doi: 10.3390/ma13010142.
23. M. Bashirpour, M. Forouzmehr, S. E. Hosseininejad, M. Kolahdouz, M. Kolahdouz, Improvement of terahertz photoconductive antenna using optical antenna array of ZnO nanorods, *Sci. Rep*., **9** (2019), 1–8. doi: 10.1038/s41598-019-38820-3.
24. B. K. Ahn, I. J. Hwang, K. S. Kim, S. C. Chae, J. W. Yu, H. L. Lee, Wide-angle scanning phased array antenna using high gain pattern reconfigurable antenna elements, *Sci. Rep*., **9** (2019), 1–13. doi: 10.1038/s41598-019-54120-2.

25. J. Li, Y. Huang, G. Wen, Compact CP antenna based on resonant Quadrifilar spiral structure for UHF RFID handheld reader, in *2017 IEEE International Symposium on Antennas and Propagation & USNC/URSI National Radio Science Meeting*, (2017), 2449–2450.
26. M. Boyarsky, T. Sleasman, M. F. Imani, J. N. Gollub, D. R. Smith, Electronically steered metasurface antenna, *Sci. Rep.*, **11** (2021), 1–10. doi: 10.1038/s41598-021-83377-9.
27. J. Li, T. A. Khan, J. Chen, M. U. Raza, A. Zhang, Design of low RCS circularly polarized patch antenna array using metasurface for CNSS adaptive antenna applications, *Materials*, **12** (2019), 1898. doi: 10.3390/ma12121898.
28. M. Faenzi, G. Minatti, D. González-Ovejero, F. Caminita, E. Martini, C. Della Giovampaola, et al., Metasurface antennas: new models, applications and realizations, *Sci. Rep.*, **9** (2019), 1–14. doi: 10.1038/s41598-019-46522-z.
29. B. Ferreira-Gomes, O. N. Oliveira, J. R. Mejía-Salazar, Chiral dielectric metasurfaces for highly integrated, broadband circularly polarized antenna, *Sensors*, **21** (2021), 2071. doi:10.3390/s21062071.
30. Z. Wang, L. Zhao, Y. Cai, S. Zheng, Y. Yin, A meta-surface antenna array decoupling (MAAD) method for mutual coupling reduction in a MIMO antenna system, *Sci. Rep*., **8** (2018), 1–9. doi: 10.1038/s41598-018-21619-z.
31. R. Kazemi, J. Palmer, F. Quaiyum, A. E. Fathy, Steerable miniaturised printed Quadrifilar helical array antenna using digital phase shifters for BGAN/GPS applications, *IET Microwaves Antennas Propag.*, **12** (2018), 1196–1204. doi: 10.1049/iet-map.2017.0959.
32. P. A. Obraztsov, V. V. Bulgakova, P. A. Chizhov, A. A. Ushakov, D. S. Gets, S. V. Makarov, et al., Hybrid perovskite terahertz photoconductive antenna, *Nanomaterials*, **11** (2021), 313. doi: 10.3390 /nano11020313.
33. Y. Han, H. Wang, Z. Wang, Y. Yao, Y. Feng, K. Hu, et al., Dual-band spiral printed quadrifilar helical antenna miniaturized by surface and inner dielectric loading, *IEEE Access*, **7** (2019), 30244–30251. doi: 10.1109/ACCESS.2019.2902308.
34. L. Sun, W. Huang, S. Gao, W. Li, X. Guo, J. Yang, Joint timekeeping of navigation satellite constellation with inter-satellite links, *Sensors*, **20** (2020), 670. doi: 10.3390/s20030670.
35. Y. Wen, J. Zhu, Y. Gong, Q. Wang, X. He, Distributed orbit determination for global navigation satellite system with inter-satellite link, *Sensors*, **19** (2019), 1031. doi: 10.3390/s19051031.
36. M. Hosseini, M. Hakkak, P. Rezaei, Design of a dual-band quadrifilar helix antenna, *IEEE Antennas Wireless Propag. Lett.*, **4** (2005), 39–42. doi: 10.1109/LAWP.2005.844142.

AIMS Press